Spatiotemporal Control of Charge +1 Topological Defects in Polar Active Matter

Birte C. Geerds,[1, 2] Abhinav Singh,[3, 4, 5] Mathieu Dedenon,[6, 2] Daniel
J. G. Pearce,[2] Frank Jülicher,[7, 1, 5, 8] Ivo F. Sbalzarini,[3, 4, 5, 8] and Karsten Kruse[6, 2]

[1]*Faculty of Physics, TU Dresden, 01069 Dresden, Germany*
[2]*Department of Theoretical Physics, University of Geneva, 1211 Geneva, Switzerland*
[3]*Faculty of Computer Science, TU Dresden, 01187 Dresden, Germany*
[4]*Max Planck Institute of Molecular Cell Biology and Genetics, 01307 Dresden, Germany*
[5]*Center for Systems Biology Dresden, 01307 Dresden, Germany*
[6]*Department of Biochemistry, University of Geneva, 1211 Geneva, Switzerland*
[7]*Max Planck Institute for the Physics of Complex Systems, 01187 Dresden, Germany*
[8]*Cluster of Excellence "Physics of Life", TU Dresden, 01307 Dresden, Germany*
(Dated: November 27, 2025)

Topological defects are a conspicuous feature of active liquid crystals that have been associated with important morphogenetic transitions in organismal development. Robust development thus requires a tight control of the motion and placement of topological defects. In this manuscript, we study a mechanism to control +1 topological defects in an active polar fluid confined to a disk. If activity is localized in an annulus within the disk, the defect moves on a circular trajectory around the center of the disk. Using an ansatz for the polar field, we determine the dependence of the angular speed and the circle radius on the boundary orientation of the polar field and the active annulus. Using a proportional integral controller, we guide the defect along complex trajectories by changing the active annulus size and the boundary orientation.

Active stress generated by the transformation of chemical energy into mechanical work is at the base of the fascinating autonomous movements seen in biological systems [1, 2]. At the molecular level, it results from the interaction of molecular motors with filamentous protein assemblies. Due to their molecular form, active stress in living matter is often anisotropic. The principal direction of the stress typically coincides with orientational order exhibited by the biological material. Macroscopic orientational order can result, for example, from the alignment of filaments [3] or of elongated cells [4, 5]. If individual filaments or cells are polarized, their alignment can result in polar or nematic orientational order.

Topological point defects are increasingly recognized to play a central role in organizing mechanical stress in biological systems. At such defects, the orientational order field is ill defined. They are characterized by their topological charge which can take half-integer values. Defects have been reported to determine the position of cell death and extrusion [6], direct the formation of cell mounds [7–9], and are essential for surface deformations that accompany the formation of mouth, foot, and tentacles during regeneration of the freshwater polyp *Hydra vulgaris* [10, 11]. Activity-induced surface deformations orchestrated by topological defects also hold promises in the design of soft robots [12].

Topological defects of charge +1 play a particular role in surface deformation. These defects are unique in that they have continuous rotational symmetry. A homogeneous local rotation of the orientation field, referred to as a change in phase, causes a +1 defect to transition between aster, spiral and vortex. For any other defect, a change in phase is simply associated with a global rotation around the defect center. Active defects of charge +1 can deform surfaces into different shapes ranging from domes to saddles depending on the phase of the defect [13]. Thus, +1 defects offer the possibility to control shapes by changing their phase. Phase changes can be performed in a restricted region around the defect, whereas the alternative, changing the topological charge of a defect, requires global changes of the orientational order.

It is thus desirable for biological and engineered systems to be able to control the arrangement of topological defects. Several proposals have been made to achieve spatio-temporal control of defect patterns in active nematics [14–17]. Such ideas have been realized in experiments on reconstituted cytoskeletal motor-filament systems [15, 18]. Similar activity patterning techniques have been shown to be applicable to Toner–Tu polar systems [19]. Defects of charge +1 are rotationally symmetric and, in contrast to half-integer defects, do not self-propel. Persistent motion of integer defects was achieved using dynamic activity patterns [19]. In spite of these efforts, achieving controlled positioning and persistent motion of +1 defects remains challenging. We explore how symmetry breaking and heterogeneous activity can work together for a precise control of such defects.

In this work, we focus on a +1 topological defect in an active polar fluid confined to a disk. We show how heterogeneous activity induces defect self-propulsion and explain its physical origin. We then leverage this mechanism for spatiotemporal defect control using a closed-loop controller. We achieve precise radial and azimuthal motion and discuss potential applications.

We investigate a 2D polar active fluid confined to a

disk using generalized hydrodynamics of active polar fluids [20, 21]. The polar field is described by the vector $\mathbf{p}$, which is associated with the free energy $F = \int f \, dA$, where

$$f = \frac{K_S}{2}(\nabla \cdot \mathbf{p})^2 + \frac{K_B}{2}(\nabla \times \mathbf{p})^2 + \frac{\chi}{2}\left(\frac{|\mathbf{p}|^4}{2} - |\mathbf{p}|^2\right) .$$ (1)

The first two terms describe how the free energy depends on local gradients of $\mathbf{p}$, with the elastic coefficients, K_S and K_B, associated with splay and bend distortions, respectively. The parameter χ controls the magnitude of a soft constraint for $|\mathbf{p}|^2 = 1$.

The dynamics of $\mathbf{p}$ are governed by

$$\frac{D}{Dt}p_\alpha = \frac{1}{\gamma}h_\alpha + \lambda p_\alpha \Delta\mu - \nu u_{\alpha\beta}p_\beta .$$ (2)

In this expression, Greek indices go from 1 to 2 and we use the convention to sum over repeated indices. We introduce the molecular field $h_\alpha = -\frac{\delta F}{\delta p_\alpha}$. The parameter γ represents the rotational viscosity, while $\Delta\mu$ denotes the chemical potential difference driving the active processes. Furthermore, the Onsager coefficient λ couples the dynamics of the polarization to $\Delta\mu$. The parameter ν is the flow alignment coefficient, which couples the polarization angle to the strain-rate tensor, defined as $u_{\alpha\beta} = \frac{1}{2}(\partial_\alpha v_\beta + \partial_\beta v_\alpha)$, where $\mathbf{v}$ is the velocity field. The co-rotational material derivative is given by $Dp_\alpha/Dt = \partial_t p_\alpha + v_\gamma \partial_\gamma p_\alpha + \omega_{\alpha\beta}p_\beta$ with the vorticity tensor $\omega_{\alpha\beta} = \frac{1}{2}(\partial_\alpha v_\beta - \partial_\beta v_\alpha)$.

We assume the system to be at low Reynolds number, and we consider the fluid motion to obey $\partial_\beta \sigma_{\alpha\beta} = 0$, where $\sigma_{\alpha\beta} = \sigma_{\alpha\beta}^v + \sigma_{\alpha\beta}^r + \sigma_{\alpha\beta}^a + \sigma_{\alpha\beta}^e + (p_\alpha h_\beta - p_\beta h_\alpha)/2$ is the sum of the viscous, reactive, active, Ericksen and antisymmetric stresses defined as

$$\sigma_{\alpha\beta}^v = 2\eta u_{\alpha\beta}$$ (3)

$$\sigma_{\alpha\beta}^r = \frac{\nu}{2}\left(p_\alpha h_\beta + p_\beta h_\alpha - p_\gamma h_\gamma \delta_{\alpha\beta}\right)$$ (4)

$$\sigma_{\alpha\beta}^a = \zeta\Delta\mu\left(p_\alpha p_\beta - \frac{1}{2}p_\gamma p_\gamma \delta_{\alpha\beta}\right)$$ (5)

$$\sigma_{\alpha\beta}^e = -P\delta_{\alpha\beta} - \frac{\partial f}{\partial(\partial_\beta p_\gamma)}\partial_\gamma p_\delta .$$ (6)

Here, P is the hydrostatic pressure. We consider an incompressible fluid, $\partial_\gamma v_\gamma = 0$, which determines P. In the disk geometry we consider, it is convenient to present the polar field $\mathbf{p}$ by the orientation angle ψ between $\mathbf{p}$ and the inward radial direction, $\cos(\psi) = -\hat{\mathbf{p}} \cdot \hat{\mathbf{r}}$, where a hat indicates a normalized vector.

We numerically solve the dynamic equations on a randomized point cloud. The differential operators are evaluated using Discretization-Corrected Particle Strength Exchange (DC-PSE) [22, 23], which was implemented in the OpenFPM library for scalable scientific computing [24] using a template-expression system for hydrodynamic equations [25]. We solve for Stokes flow with a pressure-correction algorithm to ensure incompressibility [26] and evolve the system in time using the adaptive Adams–Bashforth–Moulton time-stepping method [27] , Sect. S I [28] for details. We use the parameters given in Tab. S I [28].

At the disk boundary $r = r_o$, we implement no-slip conditions for the velocity and impose $\psi = \psi_b$ and $|\mathbf{p}| = 1$. The boundary conditions impose the presence of a topological defect of charge $+1$ in the polar field. The initial conditions for $\mathbf{p}$ are obtained by fixing the position of the defect at some $r \neq 0$ and minimizing the elastic energy F, Fig. S1a and Sect. S IV A [28]. We then add a small random angular perturbation to $\mathbf{p}$ with a magnitude that vanishes at the boundary and the defect center.

For homogeneous contractile activity ($\zeta\Delta\mu > 0$), we obtain rotating spiral defects if the activity exceeds a critical value, Sect. S IV A [28]. This is in agreement with previous reports [20]. In contrast to Ref. [20], $|\mathbf{p}|$ is not fixed in the present system. In thermodynamic equilibrium, the free energy (1) still yields $|\mathbf{p}| = 1$ away from defects. Activity, however, modifies the magnitude of the polar order. In the stationary state $\mathbf{v} = 0$ and $|\mathbf{p}| = const$, the active term in Eq. (2) leads to $|\mathbf{p}|^2 = 1 + \lambda\Delta\mu/\chi \equiv P_0^2$. In presence of a flow, the magnitude of the polar order is further affected by flow alignment.

We next investigate how the configuration changes if activity is spatially heterogeneous. We confine $\Delta\mu \neq 0$ to an annulus adjacent to the boundary of the system and leave a passive circular region with radius r_i in the center, Fig. 1a,b. We study the system in the one-constant approximation, $K \equiv K_B = K_S$, and set the boundary angle to $\psi_b = \pi/4$.

For $\Delta\mu$ larger than a critical activity $\Delta\mu_c < 0$, the defect stays in the passive region and moves to the center of the disk. The defect adopts a spiral configuration and generates a rotationally symmetric flow, Fig. S3 [28]. For $\Delta\mu < \Delta\mu_c$, the defect leaves the passive region and settles on a circular path around the center, Fig. 1c. The corresponding angular speed ω and radius r_d increase with the magnitude of the activity, Fig. 1d.

A defect circulating around the center loses its rotational symmetry, showing distinct areas of increased bend or splay, Fig. 2a. The polarization magnitude decreases towards the defect. Furthermore, $|\mathbf{p}|$ exhibits a distinct increase within the passive region as expected from the expression for P_0, Fig. 2a. The active stress around the defect leads to the steady state flow profile shown in Fig. 2b.

To better understand the conditions that give rise to the circular motion of the defect, we use an *ansatz* for the polar field associated with an off-center defect. We choose the orientation of this field to be constant along the radial direction from the defect center. Thus, the orientation of the polar field is completely determined by the boundary angle ψ_b and by the radial position r_d of
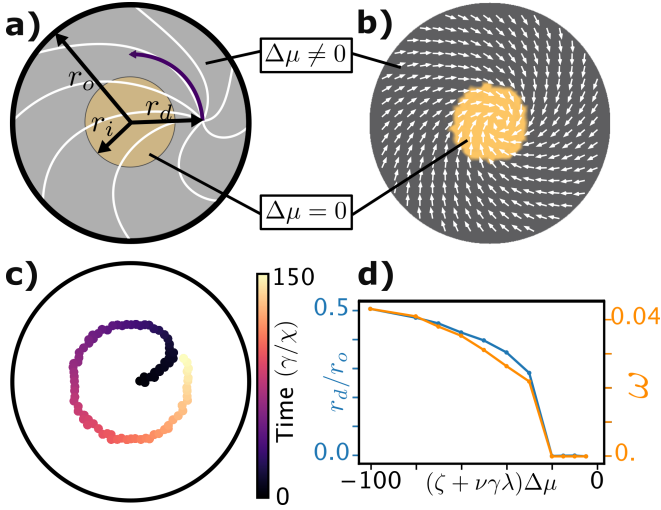
FIG. 1. Effect of heterogeneous activity patterning. **(a)** Illustration of the system. At the boundary $|\mathbf{p}| = 1$ and $\psi_b = \pi/4$. Light blue lines: polarization field lines. Dark purple curved arrow: circular segment with radius r_d. Gray shaded: region of non-zero activity $\Delta\mu \neq 0$. **(b)** Initial configuration of the numerical solver. White arrows: polarization field. Color code: orange refers to $\Delta\mu = 0$, black to $\Delta\mu \neq 0$. **(c)** Trajectory of the defect center. Color code: time. **(d)** Average distance r_d and angular speed ω of the defect center as a function of activity.
Unless specified differently $(\zeta + \nu\gamma\lambda)\Delta\mu = -100K_S/r_o^2$, $r_i/r_o = 8/25$ and $K_B = K_S$.
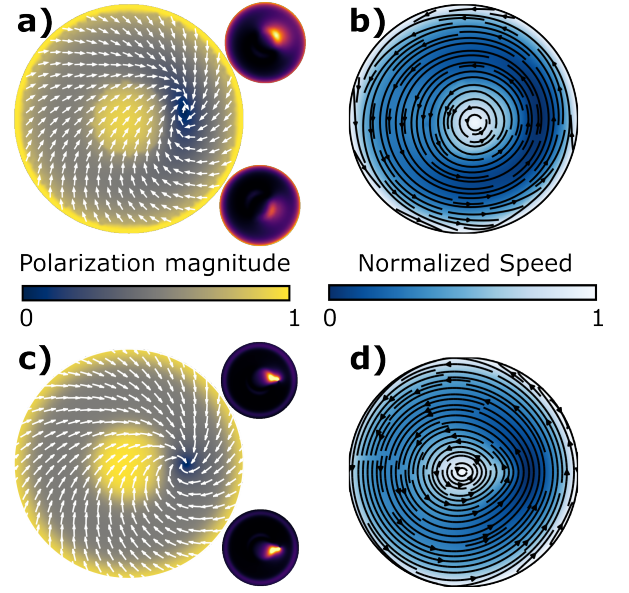

FIG. 2. Mechanism underlying circular defect movement. **(a)** Stable polarization field from simulation with heterogeneous activity and $\psi_b = \pi/4$. White arrows show the orientation and color shows the magnitude of $\mathbf{p}$. Insets: localized splay (top) and bend (bottom) distortions in the orientation field. **(b)** Stable flow field corresponding to simulation shown in (a). Black lines: streamlines, color: normalized speed. **(c)** Polarization field given by our ansatz for $\psi_b = \pi/4$ shows good agreement with (a). Insets: same as (a). $\Delta P = 0.5$, $r_p = r_o/20$ **(d)** Stokes flow field calculated from the active force around polar field shown in (c). This shows good agreement with (b).

the defect, Sect. S II [28]. We approximate the modulus of the polarization field as $|\mathbf{p}| = p_0(r)(1 - \exp\{-\rho/\varepsilon\})$, where ρ is the distance to the defect center. The characteristic length ε is determined by the parameters K and χ, $\varepsilon^2 \sim K/\chi$. For the expression of p_0, we choose $p_0 = 1 + \frac{\Delta P}{1+\exp[-(r-(r_o-2r_p))/r_p]} - \frac{\Delta P}{1+\exp[-(r-r_i)/r_p]}$. It defines the extension of the defect core, where the magnitude of the polar field is smaller than its preferred value P_0. Finally, we use ΔP and r_p as fitting parameters to match our *ansatz* with the numerical results, Fig. 2a,c.

From the *ansatz* for the polar field we can compute the active force density $\mathbf{f}$ by evaluating the divergence of the active stress, Sect. S II [28]. The magnitude of $\mathbf{f}$ depends on the radial position of the defect and increases linearly with the activity. We then calculate the Stokes flow for this force field using the two-dimensional Oseen tensor [29, 30], Sect. S III [28] for details. Our analytical and numerical results show good agreement, Fig. 2b,d.

The motion of the defect is due to advection by the flow field originating from a combination of active, elastic and viscous forces. We use our *ansatz* to estimate the elastic energy as a function of the position of the defect. The potential depends only on the radial position of the defect and has a minimum at $r_d = r_{\mathbf{min}}$, Fig. 3a. The elastic energy depends on P_0, which depends on activity. Thus, the elastic energy depends on the radius of the

passive region r_i. Below a critical value of r_i, $r_{\mathbf{min}} = 0$. Above this value $r_{\mathbf{min}}$ increases monotonically with r_i, Fig 3b. The minimum results from two competing aspects: As the defect approaches the disk boundary, the gradient terms in the elastic energy increase. In contrast, as the defect enters the passive region, the term in the elastic energy proportional to χ increases, because P_0 is larger in the passive than in the active region. There is a second critical value of r_i, above which there is a second minimum at $r_d = 0$.

We can estimate the active force on the defect by integrating $\nabla \cdot \sigma^a$ over the defect core, Sect. S II [28]. The magnitude of this force depends on the radial position of the defect and increases linearly with the activity. The active force is oriented at an angle $2\psi_b$ to the disk's radial direction. This results in an azimuthal component proportional to $\sin(2\psi_b)$ which drives the defect along a circular path around the center of the disk. The angular speed ω obtained from numerics is proportional to $\sin(2\psi_b)$, Fig. 3c. Importantly, by fixing the boundary angle ψ_b it is possible to control the orientation of the active force on the defect and thus its radial position r_d, Fig. 3d.
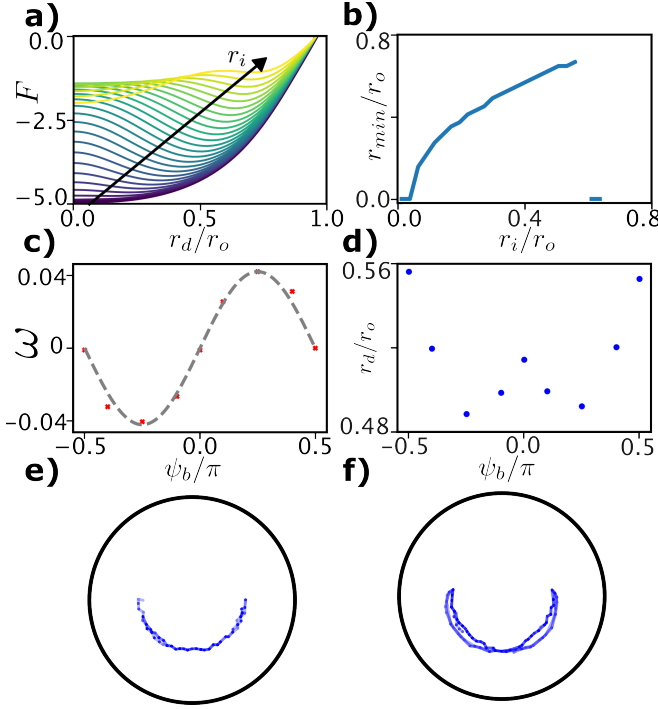
We can leverage the dependence of the active force

FIG. 3. Controlling defect motion with boundary angle. **(a)** Profile of the elastic potential F associated with placing the defect at radius r_d for different values of $r_i \in \{0., 0.65\}$ using the ansatz described in the text. **(b)** Location of the minimum in the elastic potential as a function of r_i. **(c)** Angular speed of the defect as a function of boundary angle. **(d)** Radial position of the defect as a function of boundary angle. **(e)** Oscillating defect by switching boundary angle between $\psi_b = \pm\pi/4$ and using $\psi_b = 0$, Tab. S II [28], as an intermittent value to stop the defect before return. **(f)** Defect tracing a figure eight pattern by switching between boundary angle $\psi_b = (0.45 \pm 0.25)\pi$, Tab. S III [28].

on the boundary angle ψ_b to control the defect's motion around the disk center. We can guide the defect back and forth on an arc at constant radius r_d by alternating ψ_b between $\pm\pi/4$, Tab. S II [28], Fig. 3e. If instead we periodically switch ψ_b between $(0.45 \pm 0.25)\pi$, Tab. S III [28], we introduce a radial component to the active force which allows the defect to move slightly up and down the elastic potential. This leads to the defect tracing a figure eight pattern and shows the potential of this technique, Fig. 3f. Using only the active force to guide the defect has two key weaknesses, though. First, the azimuthal motion is coupled to the radial position, thus one cannot control them independently. Second, we can only access a narrow range of radii, Fig. 3d, which leads to narrow patterns, Fig. 3f.

To overcome the limitations of controlling the defect through the boundary angle alone, we utilize the radius r_i of the passive region as a second control parameter. Controlling the radial position of the defect is more complex than controlling the angular speed, as radial active

forces must balance with the asymmetric well of the elastic potential. For this reason we chose to implement a feedback controller that modulates r_i over time to target a specific radial position of the defect.

We opt for a proportional–integral controller (PI-Controller) [31]. We define a target radius for the defect, here denoted r_d^*. The error in the target observable is calculated as $r_d - r_d^*$, and the control parameter r_i is updated proportional to the instantaneous and the time-integrated error, Fig. 4a. This approach allows us to avoid asymptotic deviations from the target value at steady state [31]. The parameters of the PI-controller must be carefully tuned to achieve the desired control, Sect. S I C [28].

In Figure 4b we demonstrate the efficacy of controlling the radial position of the defect with the PI controller. We initialize the system with a defect at $r_d/r_o = 12/25$ and $r_i/r_o = 8/25$; the target radius is fixed at $r_d^*/r_o = 9/25$. After an initial transient period of around $250\gamma/\chi$, we reach $r_d \approx r_d^*$. Once the target radius has been reached, the angular speed of the defect remains constant. We change the boundary angle at times 500, 1000, and $1500\gamma/\chi$ and the target radius r_d^* at time $1200\gamma/\chi$. Changes in the radial position r_d following changes in ψ_b are rapidly compensated by the PI controller, Fig. 4b. When changing the target radius r_d^*, the direction of circular defect motion remains unchanged whereas its speed changes. This demonstrates that we can independently control the defect's radial position r_d and its angular speed by using the PI controller and adjusting the boundary angle ψ_b.

The enhanced control of the defect made possible by the PI controller allows us to generate more complex patterns that were previously not possible. We demonstrate this by generating a closed loop with right angle corners, Fig. 4c, Tab. S IV [28], and a hanagata shape, Fig. 4d, Tab. S V [28]. Even more complex patterns would be possible using appropriate sequences of target radii and boundary conditions.

In summary, we investigated the behavior of active polar fluids confined to a 2D disk with a single topologically constrained +1 defect. For a heterogeneous activity pattern, the defect moves in a circle around the center. The circular motion depends on the boundary angle of the polar field and the size of the active annulus. Based on these dependencies we imposed target trajectories on the defect by means of a PI Controller.

Combining heterogeneous activity patterns [14–17, 19] with changes in the boundary conditions gives unprecedented possibilities for controlling the motion of individual defects. For an experimental implementation of this control principle we suggest to consider cell monolayers on patterned substrates [8, 32–34]. We expect this novel control principle to be also applicable in more complex domain shapes than the disc considered here. Given the importance of topological defects in organismal develop-
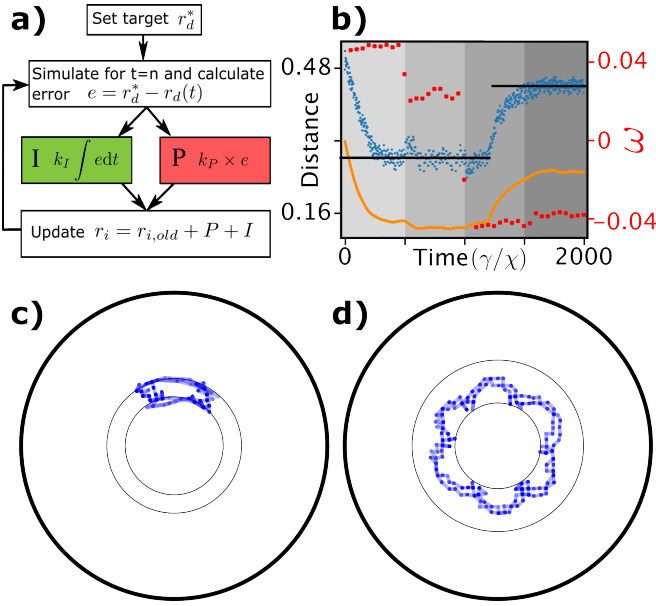
FIG. 4. Dynamic feedback control of the defect location. **(a)** Schematic of the PI-Controller. The controller maintains the radial distance of the defect at a desired setpoint r_d^* by dynamically adjusting the radius of the passive core, r_i. For each r_i, the system is simulated for $n = 50$ time steps to determine the resulting effective r_d, which yields the error that is fed back into the controller. The new r_i is calculated as $r_i = r_{i,old} + P + I$, where the P denotes the proportional part and I the integral part of the controller. $k_P = 10^{-3}$ and $k_I = 9 \cdot 10^{-3}$. **(b)** Independently controlling r_d and azimuthal motion of a defect. The setpoint changes from $r_d^*/r_o = 7/25$ to $r_d^*/r_o = 11/25$ at time step 1200 (indicated by black horizontal lines). Meanwhile, the boundary angle increases each $500\gamma/\chi$ by $\pi/5$ starting from $\psi_b = \pi/4$ (indicated by gray background). **(c)** Path of a defect tracing a closed loop with right angle corners, Tab. S IV [28]. **(d)** Path of a defect tracing a hanagata shape with internal angles over $180°$ and curved edges, Tab. S V [28].
Circles in c) and d) correspond to the extreme values for r_d^*.

ment [8, 10, 11], combining activity patterns with boundary conditions could have important implications for biological morphogenesis.

———

[1] J. Prost, F. Jülicher, and J. F. Joanny, Active gel physics, Nature Physics **11**, 111 (2015).

[2] L. Balasubramaniam, R.-M. Mège, and B. Ladoux, Active nematics across scales from cytoskeleton organization to tissue morphogenesis, Current Opinion in Genetics & Development **73**, 101897 (2022).

[3] T. Sanchez, D. T. N. Chen, S. J. DeCamp, M. Hey-mann, and Z. Dogic, Spontaneous motion in hierarchically assembled active matter, Nature **491**, 431 (2012), 1301.1122.

[4] H. Gruler, U. Dewald, and M. Eberhardt, Nematic liquid crystals formed by living amoeboid cells, The European Physical Journal B - Condensed Matter and Complex Systems **11**, 187 (1999).

[5] G. Duclos, S. Garcia, H. G. Yevick, and P. Silberzan, Perfect nematic order in confined monolayers of spindle-shaped cells, Soft Matter **10**, 2346 (2014).

[6] T. B. Saw, A. Doostmohammadi, V. Nier, L. Kocgozlu, S. Thampi, Y. Toyama, P. Marcq, C. T. Lim, J. M. Yeomans, and B. Ladoux, Topological defects in epithelia govern cell death and extrusion, Nature **544**, 212 (2017).

[7] K. Kawaguchi, R. Kageyama, and M. Sano, Topological defects control collective dynamics in neural progenitor cell cultures, Nature **545**, 327 (2017).

[8] P. Guillamat, C. Blanch-Mercader, G. Pernollet, K. Kruse, and A. Roux, Integer topological defects organize stresses driving tissue morphogenesis, Nature Materials **21**, 588 (2022).

[9] K. Endresen, A. Murali, B. Geerds, D. J. G. Pearce, and F. Serra, Actuation of cell sheets in 3d (2025), arXiv:2411.17834 [cond-mat.soft].

[10] Y. Maroudas-Sacks, L. Garion, L. Shani-Zerbib, A. Livshits, E. Braun, and K. Keren, Topological defects in the nematic order of actin fibres as organization centres of Hydra morphogenesis, Nature Physics **17**, 251 (2021).

[11] Y. Ravichandran, M. Vogg, K. Kruse, D. J. G. Pearce, and A. Roux, Topology changes of Hydra define actin orientation defects as organizers of morphogenesis, Science Advances **11**, eadr9855 (2025).

[12] V. A. Webster-Wood, M. Guix, N. W. Xu, B. Behkam, H. Sato, D. Sarkar, S. Sanchez, M. Shimizu, and K. K. Parker, Biohybrid robots: recent progress, challenges, and perspectives, Bioinspiration & Biomimetics **18**, 015001 (2022).

[13] D. J. G. Pearce, S. Gat, G. Livne, A. Bernheim-Groswasser, and K. Kruse, Programming active metamaterials using topological defects, arXiv (2020), 2010.13141.

[14] M. M. Norton, P. Grover, M. F. Hagan, and S. Fraden, Optimal Control of Active Nematics, Physical Review Letters **125**, 178005 (2020), 2007.14837.

[15] R. Zhang, S. A. Redford, P. V. Ruijgrok, N. Kumar, A. Mozaffari, S. Zemsky, A. R. Dinner, V. Vitelli, Z. Bryant, M. L. Gardel, and J. J. d. Pablo, Spatiotemporal control of liquid crystal structure and dynamics through activity patterning, Nature Materials **20**, 875 (2021), 1912.01630.

[16] S. Shankar, L. V. D. Scharrer, M. J. Bowick, and M. C. Marchetti, Design rules for controlling active topological defects, Proceedings of the National Academy of Sciences **121**, 10.1073/pnas.2400933121 (2024), 2212.00666.

[17] C. Floyd, A. R. Dinner, and S. Vaikuntanathan, Tailoring interactions between active nematic defects with reinforcement learning, Soft Matter **21**, 4488 (2025).

[18] K. Nishiyama, J. Berezney, M. M. Norton, A. Aggarwal, S. Ghosh, M. F. Hagan, Z. Dogic, and S. Fraden, Closed-loop control of active nematic flows, arXiv 10.48550/arxiv.2408.14414 (2024), 2408.14414.

[19] S. Ghosh, C. Joshi, A. Baskaran, and M. F. Hagan, Spatiotemporal control of structure and dynamics in a polar

active fluid, Soft Matter **20**, 7059 (2024).

[20] K. Kruse, J.-F. Joanny, F. Jülicher, J. Prost, and K. Sekimoto, Asters, vortices, and rotating spirals in active gels of polar filaments., Phys. Rev. Lett. **92**, 078101 (2004).

[21] K. Kruse, J. F. Joanny, F. Jülicher, J. Prost, and K. Sekimoto, Generic theory of active polar gels: a paradigm for cytoskeletal dynamics., The European physical journal. E, Soft matter **16**, 5 (2005).

[22] B. Schrader, S. Reboux, and I. F. Sbalzarini, Discretization correction of general integral PSE operators for particle methods, Journal of Computational Physics **229**, 4159 (2010).

[23] A. Singh, A. Foggia, P. Incardona, and I. F. Sbalzarini, A Meshfree Collocation Scheme for Surface Differential Operators on Point Clouds, Journal of Scientific Computing **96**, 89 (2023).

[24] P. Incardona, A. Leo, Y. Zaluzhnyi, R. Ramaswamy, and I. F. Sbalzarini, OpenFPM: A scalable open framework for particle and particle-mesh codes on parallel computers, Comput. Phys. Commun. **241**, 155 (2019).

[25] A. Singh, P. Incardona, and I. F. Sbalzarini, A C++ expression system for partial differential equations enables generic simulations of biological hydrodynamics, Eur. Phys. J. E **44**, 117 (2021).

[26] A. Singh, P. H. Suhrcke, P. Incardona, and I. F. Sbalzarini, A numerical solver for active hydrodynamics in three dimensions and its application to active turbulence, Phys. Fluids **35**, 105155 (2023).

[27] A. Singh, L. Kraatz, S. Yaskovets, P. Incardona, and I. F. Sbalzarini, Integrating odeint time stepping into openfpm for distributed and gpu accelerated numerical solvers (2025), arXiv:2309.05331 [cs.MS].

[28] See supplemental material for additional figures, tables, calculations and computational details, [URL will be provided by publisher], which includes Ref. [18, 20, 22–27, 29, 30].

[29] L. Giomi, M. J. Bowick, P. Mishra, R. Sknepnek, and M. Cristina Marchetti, Defect dynamics in active nematics, Philosophical Transactions of the Royal Society A: Mathematical, Physical and Engineering Sciences **372**, 20130365 (2014).

[30] R. Di Leonardo, S. Keen, F. Ianni, J. Leach, M. Padgett, and G. Ruocco, Hydrodynamic interactions in two dimensions, Physical Review E—Statistical, Nonlinear, and Soft Matter Physics **78**, 031406 (2008).

[31] H. P. Geering, *Regelungstechnik: Mathematische Grundlagen, Entwurfsmethoden, Beispiele*, 6th ed. (Springer, 2013).

[32] Z. Zhao, H. Li, Y. Yao, Y. Zhao, F. Serra, K. Kawaguchi, H. Zhang, and M. Sano, Integer topological defects offer a methodology to quantify and classify active cell monolayers, Nature Communications **16**, 2452 (2025).

[33] S. Coyle, B. Doss, Y. Huo, H. R. Singh, D. Quinn, K. Jimmy Hsia, and P. R. LeDuc, Cell alignment modulated by surface nano-topography – Roles of cell-matrix and cell-cell interactions, Acta Biomaterialia **142**, 149 (2022).

[34] K. D. Endresen, M. Kim, M. Pittman, Y. Chen, and F. Serra, Topological defects of integer charge in cell monolayers, Soft Matter **17**, 5878 (2021).